



## Developing a temporally land cover-based look-up table (TL-LUT) method for estimating land surface temperature based on AMSR-E data over the Chinese landmass



Ji Zhou<sup>a,b,\*</sup>, Fengnan Dai<sup>a</sup>, Xiaodong Zhang<sup>a</sup>, Shaojie Zhao<sup>b</sup>, Mingsong Li<sup>a</sup>

<sup>a</sup> School of Resources and Environment, University of Electronic Science and Technology of China, Chengdu 611731, China

<sup>b</sup> State Key Laboratory of Remote Sensing Science, Research Center for Remote Sensing and GIS, and School of Geography, Beijing Normal University, Beijing 100875, China

### ARTICLE INFO

#### Article history:

Received 4 April 2014

Accepted 1 July 2014

#### Keywords:

Land surface temperature  
Passive microwave remote sensing  
AMSR-E  
MODIS  
Land cover

### ABSTRACT

The land surface temperature (LST) is an important parameter when studying the interface between the atmosphere and the Earth's surface. Compared to satellite thermal infrared (TIR) remote sensing, passive microwave (PMW) remote sensing is better able to overcome atmospheric influences and to estimate the LST, especially in cloudy regions. However, methods for estimating PMW LSTs at the country and continental scales are still rare. The necessity of training such methods from a temporally dynamic perspective also needs further investigations. Here, a temporally land cover based look-up table (TL-LUT) method is proposed to estimate the LSTs from AMSR-E data over the Chinese landmass. In this method, the synergies between observations from MODIS (Moderate Resolution Imaging Spectroradiometer) and AMSR-E (Advanced Microwave Scanning Radiometer for EOS), which are onboard the same Aqua satellite, are explored. Validation with the synchronous MODIS LSTs demonstrates that the TL-LUT method has better performances in retrieving LSTs with AMSR-E data than the method that uses a single brightness temperature in 36.5 GHz vertical polarization channel. The accuracy of the TL-LUT method is better than 2.7 K for forest and 3.2 K for cropland. Its accuracy varies according to land cover type, time of day, and season. When compared with the in-situ measured LSTs at four sites without urban warming in the Tibet Plateau, the standard errors of estimation between the estimated AMSR-E LST and in-situ measured LST are from 5.1 K to 6.0 K in the daytime and 3.1 K to 4.5 K in the nighttime. Further comparison with the in-situ measured air temperatures at 24 meteorological stations confirms the good performance of the TL-LUT method. The feasibility of PMW remote sensing in estimating the LST for China can complement the TIR data and can, therefore, aid in the generation of daily LST maps for the entire country. Further study of the penetration of PMW radiation would benefit the LST estimations in barren and other sparsely vegetated environments.

© 2014 The Authors. Published by Elsevier B.V. This is an open access article under the CC BY-NC-ND license (<http://creativecommons.org/licenses/by-nc-nd/3.0/>).

### Introduction

As a key parameter of the land surface and atmosphere interface, land surface temperature (LST) has important influences on the Earth's surface environment and has been used extensively

in research areas such as agriculture, hydrology, ecology, meteorology, and climate (e.g., Jia and Li, 2006; Zhou et al., 2011a). Compared with the surface temperature measurements taken at ground sites, LSTs derived from satellite remotely sensed data have many benefits, e.g., broader spatial extent and denser spatial sampling intervals. Therefore, there has been great interest in estimating LSTs with required accuracies and spatiotemporal resolutions based on satellite remotely sensed data since the 1970s (Dash et al., 2002; Zhou et al., 2012; Li et al., 2013).

Most methods proposed in the LST estimation literature are based on thermal remotely sensed data. Some examples of classical algorithms used in this methodology are the split-window algorithms for sensors with two or more thermal infrared (TIR) channels

\* Corresponding author at: School of Resources and Environment, University of Electronic Science and Technology of China, Chengdu 611731, China. Tel.: +86 28 61831571; fax: +86 28 61831571.

E-mail addresses: [jzhou233@uestc.edu.cn](mailto:jzhou233@uestc.edu.cn) (J. Zhou), [daifengnan\\_abc@163.com](mailto:daifengnan_abc@163.com) (F. Dai), [bobtennis@sina.com](mailto:bobtennis@sina.com) (X. Zhang), [shaojie.zhao@bnu.edu.cn](mailto:shaojie.zhao@bnu.edu.cn) (S. Zhao), [lms0102@163.com](mailto:lms0102@163.com) (M. Li).

(e.g., Becker and Li, 1990; Wan and Dozier, 1996; Zhou et al., 2013, 2014), the temperature and emissivity separation algorithms for sensors with multiple TIR channels (e.g., Gillespie et al., 1998), and the single channel algorithms for sensors with one TIR channel (e.g., Qin et al., 2001; Jiménez-Muñoz and Sobrino, 2003; Zhou et al., 2011b). Readers are encouraged to refer to Li et al. (2013) for details. The research related to thermal remote sensing has promoted the study of land surface processes, and the LSTs derived by such methods have been used to model regional and global climate change. However, one of the most critical drawbacks of using TIR remote sensing to estimate LST is that this type of remotely sensed data is influenced by weather and atmospheric effects. Currently, valid LSTs cannot be determined under cloudy conditions. For example, over 60% of the areas in the Moderate Resolution Imaging Spectroradiometer (MODIS) LST products are contaminated by weather effects, especially cloud cover (Chen et al., 2011). The inefficiency and inaccuracy of TIR remote sensing methods is much more apparent in frequently cloudy areas, e.g., south China and the Amazon rainforest.

Compared with TIR remote sensing, passive microwave (PMW) remote sensing is better able to overcome the atmospheric influences. PMW radiation from the land surface can penetrate cloud cover and reach the satellite sensor with less attenuation. Many PMW sensors on board various satellite platforms have multi-channels with both horizontal and vertical polarizations, e.g., the Special Sensor Microwave/Imager (SSM/I) on board the Defense Meteorological Satellite Program (DMSP) satellite, the Advanced Microwave Scanning Radiometer for EOS (AMSR-E) on board the Aqua satellite, and the Advanced Microwave Scanning Radiometer 2 (AMSR2) on board the Global Change Observation Mission 1st-Water "SHIZUKU" satellite (GCOM-W1). Therefore, satellite PMW sensors provide a good data source for estimating the LST at macro-scales. In addition, some of these sensors were launched in the 1970s, making it possible to generate a long-term record of LSTs at both the continental and global scales.

The methods for estimating PMW LST can be divided into the following three categories: the empirical and statistical methods, the semi-empirical methods, and the physical methods (Li et al., 2013). The first category is the most studied of the three. For example, McFarland et al. (1990) developed empirical equations for retrieving LST of agricultural land, dry soil, and wet soil from SSM/I data. The results of this analysis indicated that a 37 GHz vertically polarized channel performed best for retrieving LST data. Li et al. (1998) constructed an empirical equation for LST inversion over Eastern China from SSM/I data by analyzing the correction of each channel to surface water, atmospheric water vapor and atmospheric cloud particles. Owe and Van De Griend (2001) found that the 37 GHz vertically polarized brightness temperature could be used to predict the LST with a high accuracy. Holmes et al. (2009) analyzed global results and found that the 37 GHz vertically polarized channel was the best channel for retrieving LST data, and they then developed the empirical algorithm for global LST retrieval. Chen et al. (2011) established regression relationships between AMSR-E brightness temperatures and meteorological observation data during the snow disaster period in Guangdong Province, China in 2008. In that study, the ground surface was classified with the microwave polarization difference index (MPDI), and the regression equation for LST retrieval was trained for each MPDI level. By examining in-situ measured soil temperatures at 0.2 cm depth at Naqu in the Qinghai-Tibet Plateau and the brightness temperatures of AMSR-E, Salama et al. (2012) confirmed a linear relationship similar to the one reported by Holmes et al. (2009).

The second category, semi-empirical methods, relies on the radiative transfer equation (RTE) of the PMW region and the correlations between parameters (e.g., emissivities) of different

channels. For example, Fily et al. (2003) found significant linear relationships between SSM/I microwave surface emissivities at horizontal and vertical polarizations over snow and ice-free land surfaces. This finding enabled the simplification of the RTEs, and then the LST was calculated based on these simplifications. By formulating the relationship between emissivities and the ratio of horizontal and vertical polarized brightness temperatures, Gao et al. (2008) proposed a so-called polarization ratio (PR) method using the AMSR-E data of the Amazon rainforest. Royer and Poirier (2010) determined the LST by constructing the empirical relationship between emissivities at both vertical and horizontal polarizations of 37 GHz from SMMR and SSM/I data of North America. Compared with the empirical and semi-empirical methods, the third method category for estimating PMW LST has a more solid physical basis and is not limited to particular regions. For example, Basist et al. (1998) constructed the LST estimation method by analyzing the relationships between emissivities of different channels from SSM/I data.

Although the empirical and semi-empirical methods are limited to the study areas where they are trained, they have several advantages. First, they are easy to implement within various scientific communities and previous research has proven that such methods can achieve highly accurate results. Second, they are convenient in that they can easily be revised and applied to other areas. Third, these methods may often be preferred by users who are interested in a study area where current physical methods are not yet applicable. However, some drawbacks still remain for this category of method. Such methods for applications at the country and continental scales are still rare. In addition, although literatures have reported that the 37 GHz vertically polarized channel is good for estimating PMW LSTs, describing the complicated linkages between PMW radiations and surface temperatures of different land cover (LC) types may require more different channels or combinations of channels, as found by Chen et al. (2011). Furthermore, the varying physical features of land surfaces in the intra-annual cycle make the necessity of training such methods from a temporally dynamic perspective needs further investigations.

In this study, the Chinese landmass is selected as the study area for estimating the LST from AMSR-E observations. The potentiality that the same satellite carries both the AMSR-E and MODIS sensors is explored. We select this study area for two main reasons. The first reason is that China displays a deteriorating environment and has been the victim of severe climate disasters in recent years. The second reason is that frequent cloud coverage over China, especially over south China and its surrounding areas, limits the applicability of TIR remote sensing in deriving LSTs. The main objective of this study is to develop a temporally land cover-based look-up table (TL-LUT) method for estimating PMW LST with accuracy comparable to the MODIS LST product, which exhibits robust performance and accurate results and has been used extensively by scientific communities. The TL-LUT method belongs to the first category method for estimating PMW LST. Therefore, it is easy and convenient for actual applications.

## Datasets and preprocessing

The datasets used in the present study are composed of AMSR-E brightness temperature data and the MODIS surface products. These two datasets are used to train and validate the TL-LUT method. Digital elevation model (DEM) data is also collected to assist in the selection of samples for training this method. In addition, in-situ measured LSTs and meteorological observations are used to further evaluate the method. Details of these datasets can be found in the following sections.

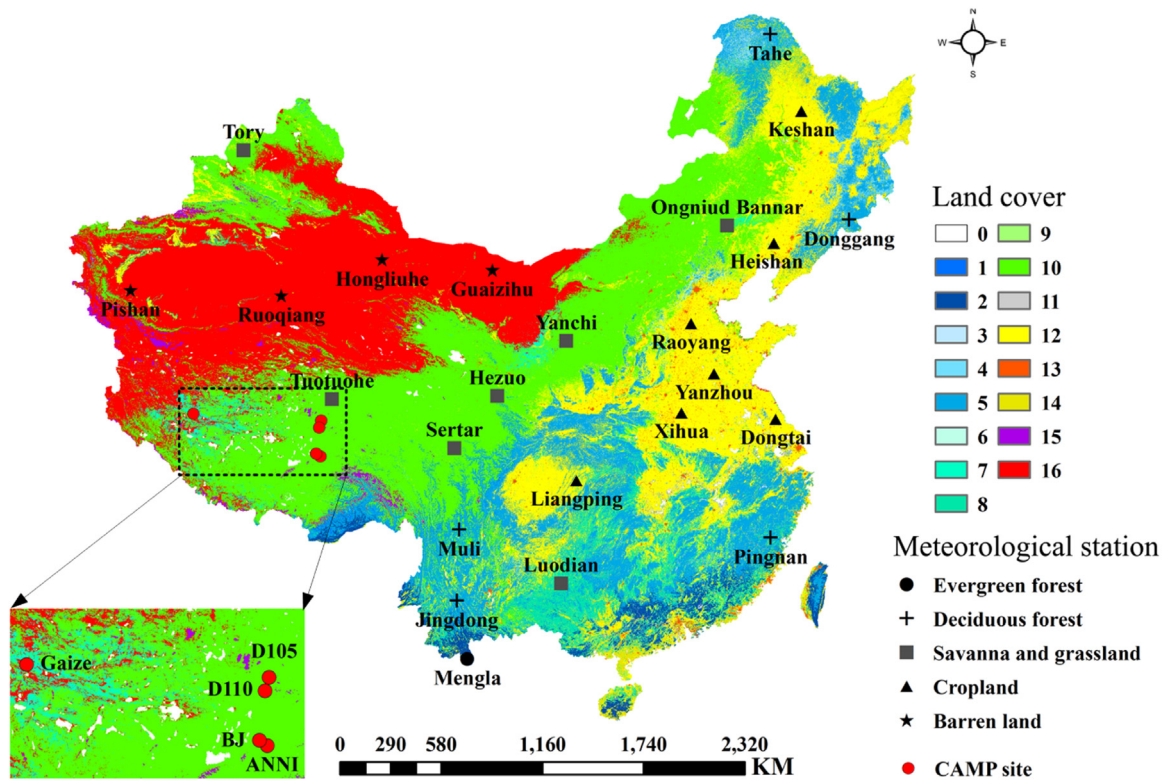


**Fig. 1.** Locations of the selected CAMP sites and meteorological stations. The LC is from the MCD12Q1 products in 2003 with a 500 m resolution. The LC codes are following: 0, water; 1, evergreen needleleaf forest; 2, evergreen broadleaf forest; 3, deciduous needleleaf forest; 4, deciduous broadleaf forest; 5, mixed forest; 6, closed shrubland; 7, open shrubland; 8, woody savanna; 9, savanna; 10, grassland; 11, permanent wetland; 12, cropland; 13, urban and built-up; 14, cropland-nature vegetation; 15, snow and ice; and 16, barren or sparsely vegetated.

#### AMSR-E data

The AMSR-E sensor is on board the Aqua satellite, which was launched in 2002 and carries one of the MODIS sensors. The Aqua overpass time is approximately 13:30 (local solar time) in ascending mode and 01:30 (local solar time) in descending mode. AMSR-E has 12 channels at 6.9 GHz, 10.7 GHz, 18.7 GHz, 23.8 GHz, 36.5 GHz, and 89.0 GHz, in both horizontal and vertical polarizations. It should be noted that the Ka band channel for many PMW radiometer is 37 GHz, except for the AMSR-E and the latest AMSR2 sensors, the corresponding channels of which are 36.5 GHz. The spatial resolution of individual measurements from AMSR-E varies from 5.4 km at 89.0 GHz to 56 km at 6.9 GHz. AMSR-E provided PMW observations of the Earth's surface at the global scale for nearly 10 years (i.e., from 2002 to 2011). Although AMSR-E stopped collecting data due to an instrument problem in October 2011, its observations serve as an important linkage between the observations of its predecessors and successors.

The AMSR-E data used here are the level 2A brightness temperatures from 2002 to 2011, downloaded from the National Snow & Ice Data Center (NSIDC). This product has a 0.25° spatial resolution. The images, which include the brightness temperatures and times for the Chinese landmass, are extracted and converted to a 25 km spatial resolution in the Albers projection to facilitate further processing. Then, the dataset in 2010 is selected as the training set to cover all the four seasons and obtain more training samples for urban and barren lands because China has experienced a rapid urbanization process in recent 10 years. The dataset in 2003 is selected for validation based on the in-situ measured LSTs. In addition, in order to test the accuracies of the PMW LSTs estimated

based on observations from the deteriorating AMSR-E sensor, the dataset in 2011 is also selected for validation.

#### MODIS surface products

The MODIS surface products used here are the daily LST/emissivity product (MYD11A1) and the 16-day vegetation indices product (MYD13A1), both in version 5, and the yearly LC product (MCD12Q1) in version 5.1. The spatial resolutions of these three types of surface products are 1000 m, 500 m, and 500 m, respectively. All available MYD11A1 products and MYD13A1 products covering the entire Chinese landmass in 2003 and 2010 are selected. In 2011, the period of the selected MYD11A1 and MYD13A1 are from January 1 to October 3. Every tile of these surface products is converted to the Albers projection through the MODIS Re-projection Tool (MRT) and the tiles are mosaicked together to cover the entire Chinese landmass.

To combine the MODIS surface products with the AMSR-E brightness temperatures, IDL programs are developed to upscale the MODIS surface products. Details regarding the processing procedure used on the LC data are presented in "Re-categorization and up-scaling of MODIS LC types". For the MYD11A1 products, the following scientific datasets (SDS) are derived: daytime and nighttime LSTs, view zenith angle (VZA), observation time, and quality control (QC). The LST images are upscaled to a 25 km resolution by spatial averaging. To measure the inner heterogeneity of the upscaled pixels, standard deviations are calculated for the LSTs of each pixel located within each 25 km box. Similar processing method as just described is used on the VZA. The observation time dataset is checked carefully to match the MODIS and AMSR-E

pixels. The QC SDS cannot be upscaled; it is used for assisting in the selection of highly reliable LSTs. The procedure for processing the MYD13A1 products is similar to that described for the MYD11A1 products. Then, the enhanced vegetation index (EVI) datasets are extracted and up-scaled, because EVI is able to detect and depict vegetation abundance under dense vegetation cover conditions.

#### Auxiliary datasets

The auxiliary datasets used in this study consist of the DEM data, in-situ measured longwave radiation, and meteorological observations. The DEM dataset has a 90 m resolution and was collected by the Shuttle Radar Topography Mission (SRTM). For use in this study, the DEM dataset was downloaded from the U.S. Geological Survey (USGS). A similar up-scaling procedure is applied to the DEM data as described for the MODIS LST products. Longwave radiation measurements were collected in 2003 by the Coordinated Enhanced Observing Period (CEOP) Asia-Australia Monsoon Project (CAMP), jointly conducted by the University of Tokyo and the Cold and Arid Regions Environmental and Engineering Research Institute, Chinese Academy of Sciences (Xu and Haginoya, 2001). We focus on the five sites that were far from large lakes and had good records of longwave radiation measurements. These sites are ANNI (elevation: 4480 m), D105 (elevation: 5038 m), D110 (elevation: 4984 m), Gaize (elevation: 4416 m), and BJ (elevation: 4509 m) (Fig. 1). The longwave radiation measurements had a temporal resolution of an hour. The landscape at D110 was grassland with canopy height less than 10 cm and the landscapes at the other four sites were barren land with canopy height less than 5 cm.

The LST is calculated according to:

$$T_s = \sqrt[4]{\frac{L^\uparrow - (1 - \varepsilon_b)L^\downarrow}{\varepsilon_b \sigma}} \quad (1)$$

where  $T_s$  is defined as the in-situ measured LST here;  $L^\uparrow$  and  $L^\downarrow$  are the outgoing and incoming longwave radiations in  $\text{Wm}^{-2}$ ;  $\sigma$  is the Stefan–Boltzmann's constant ( $5.67 \times 10^{-8} \text{Wm}^{-2} \text{K}^{-4}$ );  $\varepsilon_b$  is the broadband emissivity and it is estimated from MODIS narrowband emissivities provided by MYD11A1 products according to Liang (2004). The in-situ LSTs when AMSR-E was overpassing were calculated through linear interpolation with the hourly temperatures.

Air temperatures measured at meteorological stations are useful in evaluating the LSTs estimated from PMW data. The air temperature has good spatial representativeness and provides the possibility to minimize the scale miss-match when comparing with the PMW LST (Gao et al., 2008). Daily maximum and minimum air temperatures measured at meteorological stations in China from January 1 to December 31, 2003 were downloaded from the China Meteorological Data Sharing Service System to evaluate the estimated LST. Air temperatures were measured at a height of 1.5 m above ground level. Whether a station is selected depends on the following criteria. First, the station is located far from large cities to avoid the radio interference and urban warming. Second, it is far from lakes to avoid significant attenuation on the PMW brightness temperatures. Third, the terrain surrounding the station is flat and the LC is relatively homogenous. There are 24 ground stations obtained finally and they are scattered within the entire country (Fig. 1). These stations include one evergreen forest station, five deciduous forest stations, seven savanna and grassland stations, seven cropland stations, and four barren land stations. One should note the LC types mentioned here for these ground stations are at the AMSR-E scale and described in “Methodology”.

## Methodology

### Theoretical basis and framework of the TL-LUT method

The PMW radiance observed by the satellite remote sensor can be described according to the radiative transfer equation (Chen et al., 2011):

$$B_p(T_{bp}) = \tau_p e_p B_p(T_s) + (1 - e_p) \tau_p B_p(T_{a\text{down}}) + B_p(T_{a\text{up}}) \quad (2)$$

where the subscript  $p$  denotes the frequency;  $T_{bp}$  and  $T_s$  are the brightness temperature and LST in K, respectively;  $B_p(T_{bp})$  and  $B_p(T_s)$  are the at-sensor radiance and surface radiance in  $\text{Wm}^{-2} \text{sr}^{-1} \text{Hz}^{-1}$ , respectively;  $\tau_p$  is the atmospheric transmissivity;  $e_p$  is the land surface emissivity;  $T_a$  is the mean atmospheric temperature; and  $B_p(T_{a\text{down}})$  and  $B_p(T_{a\text{up}})$  are the atmospheric down-welling radiance and up-welling radiance in  $\text{Wm}^{-2} \text{sr}^{-1} \text{Hz}^{-1}$ , respectively. Note that LST in this study is defined as the area-weighted average of the surface temperatures of all of the LC types present in the footprint of the remote sensor.

According to the Rayleigh–Jeans approximation, Eq. (2) can be transformed into:

$$T_{bp} = \tau_p e_p T_s + (1 - e_p) \tau_p T_{a\text{down}} + T_{a\text{up}} \quad (3)$$

Eq. (3) clearly demonstrates that four parameters, including  $\tau_p$ ,  $e_p$ ,  $T_{a\text{down}}$ , and  $T_{a\text{up}}$ , are required for calculating the LST. For channels at low frequencies, e.g., 6.9 GHz and 10.7 GHz, the atmospheric influences can be ignored. Then, the LST can be calculated by dividing the brightness temperature by the surface emissivity. However, atmospheric influences should be considered for channels at higher frequencies to obtain LST estimations with satisfactory accuracy.

Eq. (3) demonstrates that the LST has a linear or approximately linear relationship with the brightness temperature. Our analysis of daytime and nighttime MODIS LSTs and corresponding AMSR-E brightness temperatures confirms such a relationship (see Fig. 2 for the daytime scatter plots). Therefore, it is possible to formulate stable and robust empirical equations for estimating the PMW LST. The aforementioned linear relationships rely on surface type and phenology (McFarland et al., 1990; Prigent et al., 1999; Holmes et al., 2009). In addition, influences on the PMW radiation from the atmosphere and surface vary throughout diurnal cycles. Therefore, the framework for the method proposed in this study can be described with the following equation:

$$T_s = B_p^{-1} \left( \frac{B_p(T_{bp}) - (1 - e_p) \tau_p B_p(T_{a\text{down}}) - B_p(T_{a\text{up}})}{\tau_p e_p} \right) = f(\mathbf{T}_b, LC, t) \quad (4)$$

where  $f$  denotes the equation for estimating the LST and it varies according to LC type at seasonal and diurnal scales;  $\mathbf{T}_b$  is the vector of PMW brightness temperatures;  $LC$  denotes the LC type;  $t$  denotes the temporal scale.

In this study, the AMSR-E brightness temperatures and the LSTs estimated from the Aqua MODIS observations are combined to deduce  $f$  in Eq. (4). This is because one of the MODIS sensors and the AMSR-E sensor provided the synchronous PMW and TIR measurements. A so-called TL-LUT method is proposed here by formulating the statistical relationship between AMSR-E brightness temperatures and their corresponding MODIS LSTs. Note that this statistical relationship may depend on LC type and varies at different temporal scales. Therefore, we are not attempt to construct a general empirical equation for all cases. Each AMSR-E pixel is flagged by its LC type. Then the statistical relationship for every LC type is analyzed and the empirical equation is trained. A chart depicting the workflow of the TL-LUT method is shown in Fig. 3. Details are presented in “Re-categorization and up-scaling of MODIS LC types” and “Extraction of training samples and realization of the TL-LUT method”.

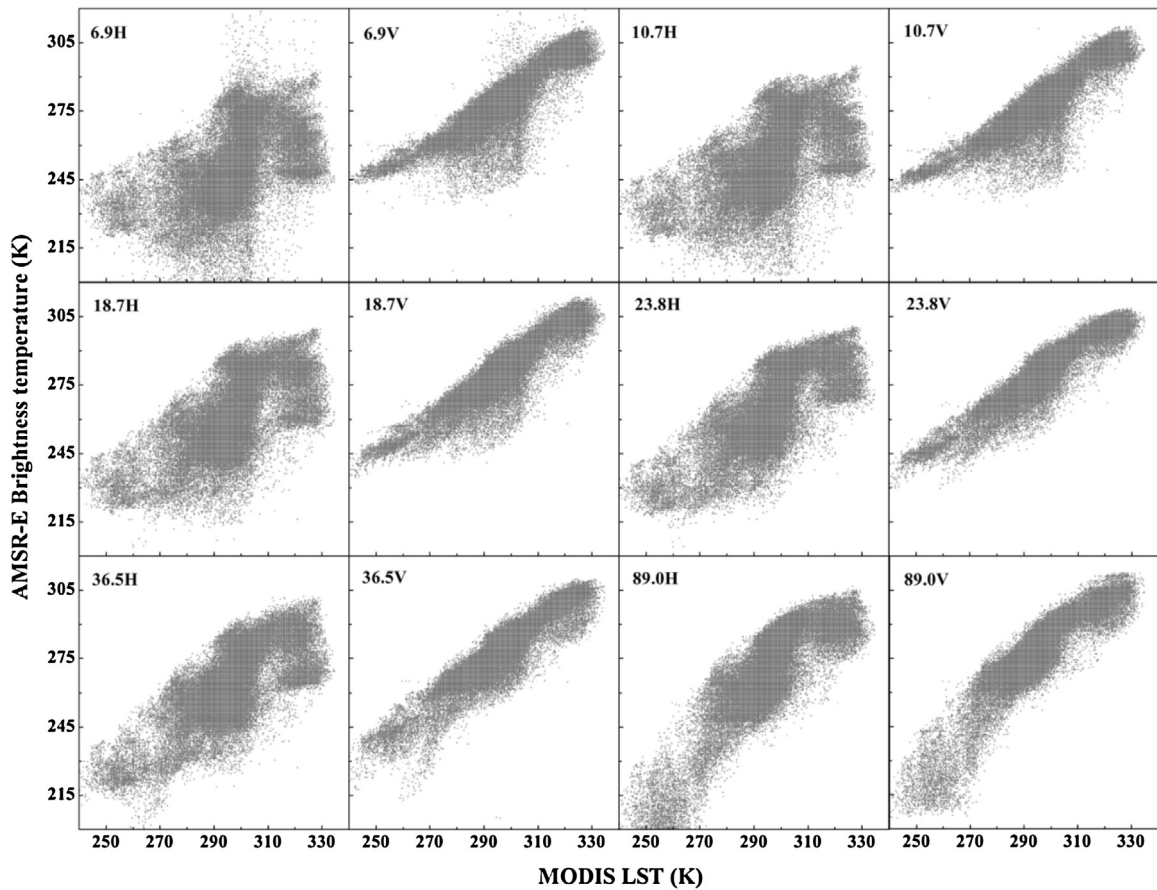


**Fig. 2.** Scatter plots between the daytime MODIS LSTs and AMSR-E horizontal and vertical polarized brightness temperatures at different frequencies. The samples are from the entire Chinese landmass in 2010.

*Re-categorization and up-scaling of MODIS LC types*

LC data is one of the basic datasets used in the development of the TL-LUT method. As described previously, the spatial resolution of the MODIS LC data is 500 m. A simple but effective procedure is used here to match MODIS LC data with the corresponding AMSR-E brightness temperature data. This procedure is composed of two stages.

The first stage is to re-categorize the MODIS LC types. The MCD12Q1 product provides LC types generated according to five classification schemes, including the IGBP global vegetation classification scheme, University of Maryland (UMD) scheme, MODIS-derived LAI/fPAR scheme, MODIS-derived Net Primary Production (NPP) scheme, and the Plant Functional Type (PFT) scheme. The LC types generated from the commonly used IGBP global vegetation classification scheme are adopted here. The establishment of

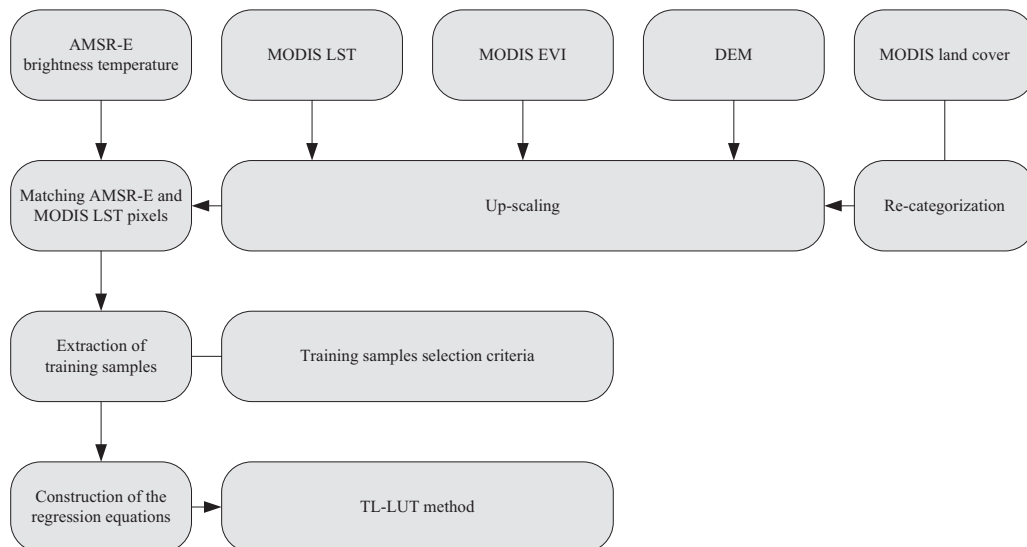


**Fig. 3.** The workflow of the TL-LUT method.

**Table 1**  
Corresponding MODIS land cover data classification codes and those after re-categorization and up-scaling.

| Code and type of MCD12Q1          | Code and definition after re-categorization and up-scaling |                  |
|-----------------------------------|--|------------------|
|                                   | For pure pixels  | For mixed pixels |
| 0 – Water                         | 0 – Water and permanent wetland                            | None pixel       |
| 11 – Permanent wetland            |  |                  |
| 1 – Evergreen needleleaf forest   | 1 – Evergreen forest                                       | 10               |
| 2 – Evergreen broadleaf forest    |  |                  |
| 3 – Deciduous needleleaf forest   | 2 – Deciduous forest                                       | 20               |
| 4 – Deciduous broadleaf forest    |  |                  |
| 5 – Mixed forest                  |  |                  |
| 6 – Closed shrubland              | 3 – Shrubland  | 30               |
| 7 – Open Shrubland                |  |                  |
| 8 – Woody savanna                 | 4 – Savanna and grassland                                  | 40               |
| 9 – Savanna                       |  |                  |
| 10 – Grassland                    |  |                  |
| 12 – Cropland                     | 5 – Cropland   | 50               |
| 14 – Cropland-nature vegetation   |  |                  |
| 13 – Urban and built-up           | 6 – Barren land  | 60               |
| 16 – Barren or sparsely vegetated |  |                  |
| 15 – Snow and ice                 | 7 – Snow and ice   | 70               |

empirical equations for every class is believed to be helpful for estimating the LST. Unfortunately, we find that there are not enough training samples for some classes due to cloud contamination of the MODIS LST products. Some classes, e.g., different types of forest, may have similar signatures on AMSR-E images, especially in a single season. For example, most PMW radiation contributing to the AMSR-E brightness temperature for deciduous needleleaf forest, deciduous broadleaf forest, and mixed forest in summer is from the canopy, due to the thick branches and leaves; in winter, the underlying soil may contribute to the PMW radiation as well as the canopy. Therefore, the 17 classes derived from the MODIS LC data are first re-categorized according to their physical characteristics. The re-categorization scheme is: water and permanent wetland are combined; evergreen needleleaf forest and evergreen broadleaf forest are combined into evergreen forest; deciduous needleleaf forest, deciduous broadleaf forest, and mixed forest are combined into deciduous forest; closed shrubland and open shrubland are combined into shrubland; woody savanna, savanna, and grassland are combined into savanna and grassland; cropland and cropland-nature vegetation are combined into cropland; urban and built-up and barren or sparsely vegetated are combined into barren land; snow and ice remains unchanged. The codes of the LC types before and after re-categorization are shown in Table 1.

In order to match the AMSR-E brightness temperatures and MODIS LSTs, the second stage is to up-scale the re-categorized LC data to the 25 km resolution. Although many mixed pixels exist at the 25 km scale, it is reasonable to assume that the aforementioned relationship is mainly influenced by the dominating LC type in the AMSR-E pixel. Therefore, the fraction of each LC type of the 500 m pixels within each AMSR-E pixel is calculated. If one LC type holds a fraction greater than a predefined threshold value, this AMSR-E pixel is assumed to be “pure” and is flagged as the type with the greatest fraction. Otherwise, this AMSR-E pixel is assumed to be a “mixed” pixel composed by the main LC type and other types. The code of a “pure” pixel is the same as the LC type that holds the greatest fraction. The code of a “mixed” pixel is a combination of the LC type that holds the greatest fraction of their areas and zero.

The predefined threshold has important influences in determining whether an AMSR-E pixel located on the edge of a land parcel is a pure pixel or a mixed pixel. We calculate the numbers of pure and mixed pixels of the entire Chinese landmass with the threshold vary from 0.5 to 0.9 with a step of 0.1. The finding is in our expectation that the numbers of pure pixels decrease and the numbers

of mixed pixels increase with higher thresholds, and vice versa. Determination of threshold is a compromise between the numbers of training samples and their homogeneity on land cover. Through a trial and error process, the threshold is set as 0.6. The numbers for pure pixels of the land cover types in order of code listed in Table 1 are 110, 132, 1553, 22, 4580, 2382, 3235, and 16, respectively.

#### *Extraction of training samples and realization of the TL-LUT method*

Establishment of the previously mentioned empirical equations relies on training samples. Each training sample is an AMSR-E pixel, which contains PWM brightness temperatures of both vertically and horizontally polarized channels at different frequencies. The LST of the AMSR-E pixel is up-scaled from the MYD11A1 LSTs. An AMSR-E pixel belongs to one of the following eight temporal cases, i.e., daytime or nighttime in a season (spring, summer, autumn, and winter). All the daily AMSR-E images and their corresponding MYD11A1 products in 2010 are scanned and the AMSR-E pixels are checked pixel by pixel. If a group of MODIS pixels are within an AMSR-E pixel and they were observed at the same time, this AMSR-E pixel is flagged as a potential training sample and its matching MODIS pixels are also recorded for further screening.

There are three main considerations in the screening process. The first consideration is the uncertainties of the MODIS LSTs, which have significant influences on accuracies of the subsequently estimated AMSR-E LSTs. Such uncertainties are influenced by many factors, e.g., the land surface emissivity, the sensor VZA, terrain, land cover type, cloud masking, and temporal condition. Although the daily MODIS LST product has a nominal accuracy than 1.0K in some cases, it still requires further validations (Wan, 2008). Due to the weakness of classification-based model in estimating the land surface emissivities in semi-arid and arid areas, the quality of the MODIS LST product may not be very good in these areas (Snyder et al., 1998; Wan, 2014). The QC information provided by the MYD11A1 products demonstrates the usefulness of the LST determined by the MODIS LST generation system. Therefore, only the samples, the QC attributes of MODIS LSTs of which are flagged as good, are selected.

The second consideration is the validness of the AMSR-E brightness temperatures of all channels. The PR, which is defined as the ratio of the horizontal to vertical brightness temperatures at the same frequency, is used here (Gao et al., 2008). PR is commonly

**Table 2**  
Retrieval equations for calculating daytime LST from AMSR-E data in summer.

| Land cover code | Regression equation   |
|-----------------|---|
| 0               | $T_S = 19.794 + 0.130T_{b6.9H} + 1.391T_{b23.8V} - 0.707T_{b36.5H} + 0.155T_{b89.0H} + 0.095(T_{b36.5V} - T_{b18.7V})^2 - 0.061(T_{b36.5V} - T_{b23.8V})^2$                                   |
| 1               | $T_S = 197.495 - 0.082T_{b10.7H} + 0.433T_{b89.0H}$   |
| 2               | $T_S = -0.859 + 0.263T_{b6.9H} + 0.211T_{b6.9V} - 1.287T_{b18.7H} + 1.413T_{b18.7V} + 0.535T_{b23.8V} + 0.087(T_{b36.5V} - T_{b23.8V})^2$   |
| 3               | $T_S = -72.290 - 1.721T_{b18.7V} + 3.047T_{b23.8V}$   |
| 4               | $T_S = 46.165 + 0.889T_{b23.8V}$  |
| 5               | $T_S = 20.368 + 0.142T_{b6.9H} - 0.107T_{b6.9V} + 0.362T_{b10.7H} + 0.114T_{b10.7V} - 0.719T_{b18.7H} - 0.389T_{b23.8H} + 1.578T_{b23.8V} - 0.001T_{b89.0H} + 0.927(T_{b36.5H} - T_{b18.7H})$ |
| 6               | $T_S = 85.025 - 0.400T_{b10.7H} + 0.789T_{b10.7V} + 0.230T_{b18.7H} - 1.199T_{b36.5V} + 0.335T_{b89.0H} + 1.010T_{b89.0V} + 0.039(T_{b36.5V} - T_{b18.7V})^2$                                 |

lower than one. Therefore, the samples with PR values higher than one at any of the six frequencies are removed.

The third consideration is the homogeneity of the AMSR-E pixels. In fact, it is extremely difficult to find a homogeneous pixel at the 25 km scale, except in deserts, large lakes, and oceans. Here, a training sample is required to be relatively homogenous at the following aspects, similar to Frey et al. (2012). First, the AMSR-E pixel is dominated by one land cover type as mentioned in “Re-categorization and up-scaling of MODIS LC types”. Second, the inner terrain of the AMSR-E pixel is flat, with the average slope of the inner MODIS pixels is lower than 2.0° and the standard deviation of the slope is lower than 0.5°. Third, the standard deviation of the LSTs of the inner MODIS pixels is lower than 5.0 K, to avoid that the AMSR-E pixel covers an area with drastic temperature variations. Fourth, the standard deviation of the EVI values of inner MODIS pixels is lower than 0.5, to remove the AMSR-E pixels covering the transitional zones of land and open water or land and snow and ice. Furthermore, if the inner MODIS pixels were observed at a view zenith angle greater than 45°, the AMSR-E pixel is removed to avoid significant thermal anisotropy effect. Note that the number of training samples decreases rapidly with stricter constraints on the aforementioned attributes. The thresholds listed here are determined through a trial-and-error process.

The training samples extracted for each land cover class in each season are used to find the mathematical expressions of the retrieval equations. The seasons are defined according to the climatic and physical features in China, as follows: spring is from March to May, summer is from June to August, autumn is from September to November, and winter is from December to the following year’s February. The daytime and nighttime cases are treated separately. Besides the AMSR-E brightness temperatures, combinations of brightness temperatures are also selected as potential predictors to correct the influences of soil moisture and atmospheric water vapor (McFarland et al., 1990). The general form of the retrieval equations is:

$$T_S = A_0 + \sum_{i=1}^6 (A_{ih}T_{bih} + A_{iv}T_{biv}) + B_1(T_{b36.5v} - T_{b18.7v}) + B_2(T_{b36.5v} - T_{b18.7v})^2 + C_1(T_{b36.5v} - T_{b23.8v}) + C_2(T_{b36.5v} - T_{b23.8v})^2 \quad (5)$$

where the subscript h and v denote the horizontal and vertical polarization; the subscript i denotes the frequencies of 6.9 GHz, 10.7 GHz, 18.7 GHz, 23.8 GHz, 36.5 GHz, and 89.0 GHz;  $A_0, A_i (i = 1, 2, \dots, 6), B_1, B_2, C_1,$  and  $C_2$  are coefficients, respectively.

To remove redundant predictors, the stepwise regression method is adopted and the entering and removing probabilities are set as 0.05 and 0.1, respectively. Then, the determined regression equations are used as the retrieval equations. One should note that there exist a number of mixed pixels in the up-scaled LC map. With the predefined threshold of 0.6, the numbers of pixels recoded as 10, 20, 30, 40, 50, 60, and 70 are 195 (1.28%), 742 (4.87%), 69 (0.45%), 1183 (7.77%), 716 (4.70%), 262 (1.72%), and 35 (0.23%), respectively; their proportions are 1.28%, 4.87%, 0.45%, 7.77%, 4.70%, 1.72%, and

0.23%, respectively. For these mixed pixels, the LSTs are calculated as the area-weighted average of the temperatures of its components, the temperatures of which are determined according to the corresponding regression equations.

**Results**

*LST retrieval equations*

The LC map of 2010 after re-categorization and up-scaling is shown in Fig. 4. Although these are some LC changes at the 500 m scale, especially in areas surrounding large cities, the LC changes at the 25 km scale can be neglected. Generally speaking, barren land, composed mainly of deserts and gobi, is distributed throughout northwest China. Savanna and grassland dominate the landscape from north China to the Qinghai–Tibet Plateau and it is the most widely distributed LC type at the 25 km scale. Cropland scatters throughout northeast China, east China, and south China. Evergreen, deciduous forest and shrubland are mainly present in south China, which is also covered by some mixed pixels of grassland and cropland. In 2010, the numbers of pixels for land cover 0–7 were 110, 132, 1553, 22, 4580, 2382, 3235, and 16, respectively. The regressions in all cases are significant at the 0.001 level, except for snow and ice due to insufficient samples. The regression statistics, including the sample sizes, coefficients of determination ( $R^2$ ), standard errors of estimation (SEE), and  $F$ -tests ( $F_{rest}$ ), are shown in Fig. 5. Due to space limitations, only the regression equations for daytime cases in the summer are listed in Table 2.

As expected, LC types with broad distribution patterns, i.e., savanna and grassland, cropland, and barren land, have more training samples than the other four types (Fig. 5(a)). The  $R^2$  value reflects the quality of a trained equation. Fig. 5(b) demonstrates that the  $R^2$  values in most cases are greater than 0.7, suggesting that the equations are trained with strong performance and stability. Comparisons between seasons show that  $R^2$  values in summer are generally lower than those in the other three seasons. This phenomenon may be resulted from several reasons. First, the MODIS TIR observations suffer from stronger atmospheric influences in summer than in other seasons due to warmer and wetter atmosphere. Such influences are difficult to completely correct with the split-window algorithm. Second, we find that fewer predictors are selected in the summer equations. Most predictors are brightness temperatures in channels at frequencies lower than 36.5 GHz, to overcome the strong atmospheric influences. This also contributes to the lower  $R^2$  values in summer. An example is the evergreen forest, the  $R^2$  value of which is 0.183 and only  $T_{b10.7v}$  and  $T_{b89.0h}$  are selected in the summer equation (Table 2).

SEE can represent the accuracy of a trained equation. As shown by Fig. 5(c), the trained retrieval equations have promising accuracies. In daytime and nighttime cases, SEE values are generally lower than 4.0 K and 3.5 K, respectively, with a few exceptions. The average values of SEEs for daytime and nighttime cases are 2.9 K and 2.5 K, respectively. A closer look in Fig. 5(c) shows that the SEE value varies according to LC type and season. The type of water and permanent wetland has higher SEE values in spring and winter than

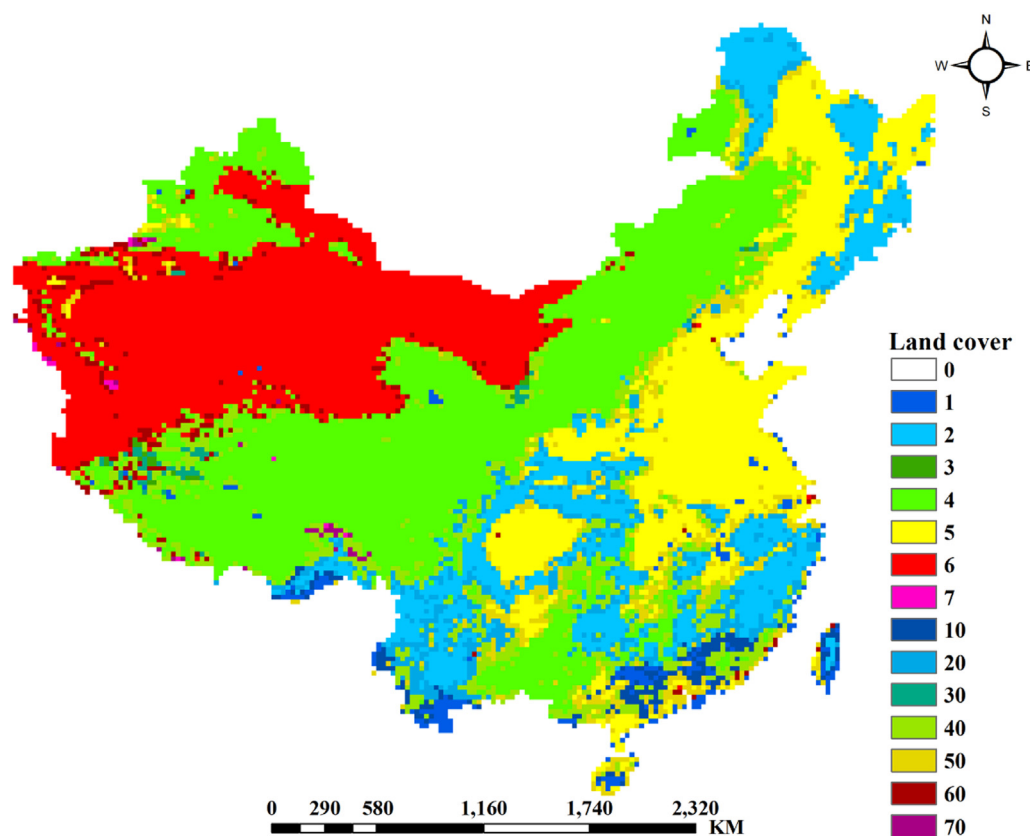


**Fig. 4.** Land cover map of 2010 after re-categorization and up-scaling. The LC codes are following: 0, water and permanent wetland with “pure” pixels; 1, evergreen forest with “pure” pixels; 2, deciduous forest with “pure” pixels; 3, shrubland with “pure” pixels; 4, savanna and grassland with “pure” pixels; 5, cropland with “pure” pixels; 6, barren land with “pure” pixels; 7, snow and ice; 10, evergreen forest with “mixed” pixels; 20, deciduous forest with “mixed” pixels; 30, shrubland with “mixed” pixels; 40, savanna and grassland with “mixed” pixels; 50, cropland with “mixed” pixels; 60, barren land with “mixed” pixels; and 70, snow and ice with “mixed” pixels.

in summer and autumn. The daytime and nighttime SEE values are 4.4 K, 4.9 K, 3.9 K, and 4.0 K in spring and winter, respectively; while the corresponding values are below 2.3 K in daytime cases and 2.6 K in nighttime conditions in summer and autumn. One possible reason is the great difference in emissivities of water and ice in winter and early spring. The PMW emissivity of ice has great variations while that of water is relatively stable.

SEE values of the forest (i.e., evergreen forest and deciduous forest) and shrubland are generally lower than 3.0 K, indicating that the surface temperatures of high vegetation can be accurately predicted with the PMW brightness temperatures. For dense vegetation, contributions to PMW radiation at ground level are mainly from the canopy, the inner temperature gradient of which is lower than the canopy and soil system. Therefore, the mixed temperature signatures acquired by the PMW sensor are prone to be similar to the skin signatures contributing to the TIR sensor. The LC types with low vegetation (i.e., savanna, grassland and cropland) and barren land have higher SEE values than the high vegetation types. One reason is that contributions to PMW radiation at ground level are from the vegetation canopy and the soil at different depths, depending on the leaf water content and the soil moisture. The difference between such signature and the signature acquired by the TIR sensor is ignorable.

The reason that the nighttime SEE values are generally lower than the daytime ones may relate to the slow spatial variations and low vertical temperature gradients of the nighttime temperature. During the nighttime, the vertical gradient of temperature is lower than that during the daytime. This decreasing vertical gradient of temperature makes the integrated temperature detected by AMSR-E is similar to that of the skin temperature detected by

MODIS, especially for landscapes with low vegetation and barren land. On the contrary, the great vertical gradient of temperature during the daytime enlarges the LST difference between the AMSR-E and MODIS.

#### Assessments of the TL-LUT method

Assessments of the TL-LUT method are essential for insuring its applicability in practical applications. In fact, validation is a difficult task especially for PMW data with coarse spatial resolutions. Comparisons between the estimated LST and the corresponding “ground truth” may be influenced by many factors, e.g., “ground truth” uncertainties and scale mismatches existing between different datasets (Zhou et al., 2012, 2014). Here, the TL-LUT method is assessed based on the synchronous MODIS LST products, the in-situ measured LSTs at five sites in the Tibet Plateau, and the daily maximum and minimum air temperatures from 24 stations in China.

#### Validation with the synchronous MODIS LST products

The MODIS LST with a 1 km resolution has a comparative spatial coverage and good accuracy for validating the AMSR-E LST. Synchronous LSTs derived from the MYD11A1 products in the Chinese landmass in 2011 are used to validate the estimated AMSR-E LSTs. It should be noted that the method used in selecting the validating samples are the same as that used in selecting the training samples described in “Extraction of training samples and realization of the TL-LUT method”. In addition, for further comparison with the TL-LUT method and the single channel method proposed by Holmes et al. (2009), validating samples with MODIS LSTs below 273.15 K

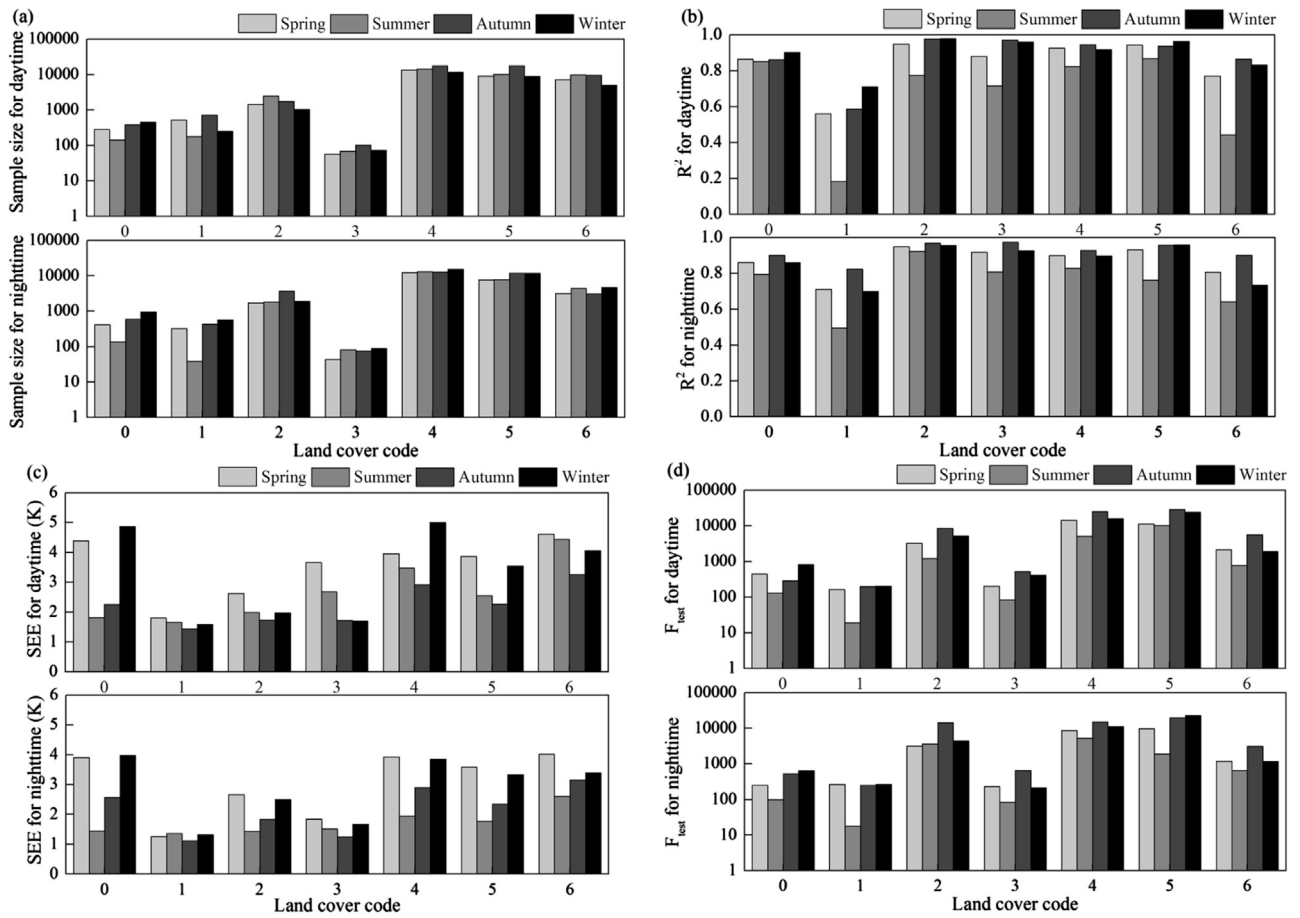


Fig. 5. Sample sizes, coefficients of determination ( $R^2$ ), standard errors of estimation (SEE), and  $F$ -test values for the regression equations in the TL-LUT method.

are removed. Therefore, the validation and comparison presented here are for unfrozen conditions.

The eventual sample sizes for daytime cases in spring, summer, autumn, and winter are 62,621, 101,267, 30,762, and 31,517, respectively; the corresponding sample sizes for nighttime cases are 20,118, 73,880, 14,020, and 10,140, respectively. The sample sizes are fewest in winter due to frequently frozen conditions. Biases of the estimated LSTs from the MODIS LSTs are calculated. The histograms of the biases for all LC types in all seasons are shown in Fig. 6. Two indicators, including the mean absolute deviation

(MAD) and root mean squared deviation (RMSD), are calculated and are listed in Tables 3 and 4.

Fig. 6 demonstrates that the biases of most daytime samples ranged from  $-12.0\text{K}$  to  $6.0\text{K}$  and the biases of most nighttime samples ranged from  $-6.0\text{K}$  to  $6.0\text{K}$ , suggesting that the retrieval equations in the nighttime conditions have better accuracies than in the daytime conditions. Most histograms present good normal distribution patterns, except for those of the daytime cases in winter and the nighttime cases in spring. The exception of the daytime case in winter is caused by poor accuracies of the AMSR-E LSTs in

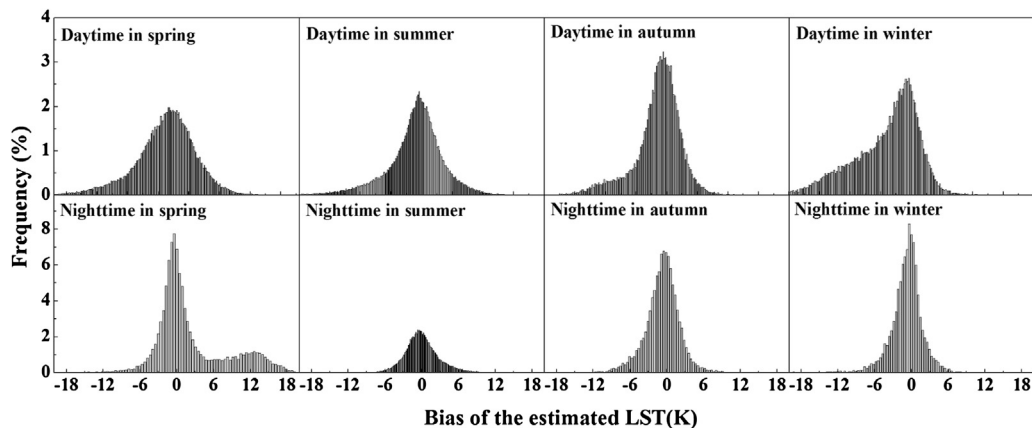


Fig. 6. Biases of the estimated daytime and nighttime AMSR-E LSTs from MODIS LSTs in different seasons for all LC types.

**Table 3**  
Mean absolute deviations (MADs) of estimated LST based on AMSR-E data for different LC types. The numbers in brackets represent MADs for the methods proposed by Holmes et al. (2009).

| Land cover type             | Daytime    |           |             |             | Nighttime  |           |           |            |
|-----------------------------|------------|-----------|-------------|-------------|------------|-----------|-----------|------------|
|                             | Spring     | Summer    | Autumn      | Winter      | Spring     | Summer    | Autumn    | Winter     |
| Water and permanent wetland | 5.0        | 2.7       | 2.1         | 3.0         | 7.0        | 2.0       | 2.5       | 2.2        |
| Evergreen forest            | 1.6 (1.9)  | 2.3 (2.2) | 1.6 (2.1)   | 1.6 (2.0)   | 1.0 (1.6)  | 3.4 (3.6) | 1.4 (2.3) | 1.1 (1.7)  |
| Deciduous forest            | 2.5 (3.4)  | 1.7 (4.1) | 1.8 (3.7)   | 2.2 (3.4)   | 2.1 (4.0)  | 1.5 (3.7) | 1.6 (4.1) | 3.9 (3.5)  |
| Shrubland                   | 7.5 (10.7) | 6.4 (9.2) | 10.3 (10.6) | 11.0 (11.9) | 3.0 (4.4)  | 1.9 (4.0) | 4.3 (4.1) | –          |
| Savanna and grassland       | 3.9 (5.6)  | 4.7 (4.8) | 3.6 (5.5)   | 6.3 (7.5)   | 10.2 (6.2) | 1.8 (5.4) | 2.6 (5.1) | 2.7 (2.9)  |
| Cropland                    | 4.2 (4.9)  | 1.9 (4.2) | 1.7 (3.6)   | 2.0 (4.8)   | 1.8 (4.7)  | 2.6 (3.9) | 1.8 (4.4) | 2.1 (6.5)  |
| Barren land                 | 5.1 (11.1) | 4.0 (8.3) | 4.4 (9.2)   | 7.7 (11.6)  | 3.5 (9.6)  | 2.2 (7.8) | 2.8 (8.2) | 7.6 (12.9) |

shrubland and barren land; the exception of the nighttime case in spring is caused by the poor accuracies in savanna and grassland. This point will be analyzed later.

Tables 3 and 4 show that the accuracy of the proposed TL-LUT method varies according to LC type, season, and time of day. Although land surfaces with large areas of water suffer from problems such as the influence of low brightness temperatures and high polarization differences, the TL-LUT method finds a robust linkage between the surface temperatures of inland lakes and the brightness temperatures of AMSR-E. As shown in Tables 3 and 4, the MAD and RMSD values of water are below 3.0 K and 3.9 K, respectively, except in spring. The MAD and RMSD values in daytime of spring are 5.0 K and 6.8 K, respectively; the corresponding values in nighttime of spring are 7.0 K and 8.9 K, respectively. This poor accuracy in spring may be because variations of water surface temperature cannot be explained completely by the selected predictors, revealed by the large SEE values presented in Fig. 5(c).

For the forest type (i.e., evergreen forest and deciduous forest), the LSTs estimated with the TL-LUT method have good accuracies in general cases. It should be noted that the LST is the canopy surface temperature in this case (Holmes et al., 2009), and its physical meaning is similar to the skin surface temperature observed by the MODIS sensor. For the evergreen forest, the daytime MAD and RMSD values are below 2.3 K and 2.7 K and the mean values are 1.8 K and 2.2 K, respectively; the nighttime MAD and RMSD values are below 3.4 K and 4.4 K and the mean values are 1.7 K and 2.3 K, respectively. High bias in the nighttime cases in the summer may be attributable to the fact that there are too few training samples, see Fig. 5(a). Although the regression equations developed by the training samples have good accuracy, the samples cannot cover every possible condition. This is the main drawback of the empirical models. For the deciduous forest, the daytime MAD and RMSD values are below 2.5 K and 3.2 K and the mean values are 2.0 K and 2.7 K; the nighttime MAD and RMSD values are below 3.9 K and 5.7 K and the mean values are 2.3 K and 3.4 K, respectively. Holmes et al. (2009) reported that the vertical polarized brightness temperature at 36.5 GHz of AMSR-E is a good predictor for estimating the forest surface temperature on a global scale and the accuracy is expected to be better than 2.5 K. Here, we find that for the Chinese landmass, the MAD ranged from 1.6 K to 2.3 K and the RMSD ranged

from 2.4 K to 3.6 K for evergreen forest, but it is unsatisfactory for the nighttime cases in the summer. For deciduous forest, the minimum MAD is 3.4 K and the minimum RMSD is 4.4 K. From our study, we conclude that retrieval equations with more predictors perform better in retrieving the canopy surface temperature with AMSR-E data than the methods that use a single brightness temperature.

The accuracy of the temperatures for sparsely vegetated surfaces (i.e., shrubland, savanna and grassland, and cropland) and barren land also vary according to the time of day and season. For shrubland, the retrieval accuracies are not acceptable except during the nighttime cases in the summer, with corresponding MAD and RMSD values of 1.9 K and 2.4 K, respectively. The poor accuracy for shrubland is because there are too few training samples, see Figs. 4 and 5(a). The MAD and RMSD values of the daytime surface temperatures of savanna and grassland in all seasons and the nighttime surface temperatures in the spring are greater than 3.6 K and 4.9 K, respectively. In the other three cases, the MADs and RMSDs are below 2.7 K and 3.6 K, respectively. The unsatisfactory performances of the regression equations for savanna and grassland are also represented by SEEs during the training process, see Fig. 5(c). However, the estimated surface temperatures show strong correlations to the MODIS LSTs. For the daytime cases, the correlation coefficients are 0.89, 0.78, 0.77, and 0.77 in the spring, summer, autumn, and winter, respectively; the correlation coefficient is 0.82 for nighttime cases in the spring. Although the surface temperature provided by MODIS is selected as the dependent variable in the training process, the variations in the surface temperature of savanna and grassland cannot be sufficiently explained by the selected brightness temperatures and band combinations. We believe that one important reason for this phenomenon is the thermal sampling of PMW remote sensing. In addition to the atmospheric effects and the PMW radiation from the grass canopy, the underlying soil (from the surface to a shallow depth) also contributes to the radiation acquired by the AMSR-E sensor. However, the TIR radiation acquired by the MODIS sensor is from the "skin" of grass leaves and their surrounding soil. During the nighttime, the vertical gradient between the temperature of the grass surface and its underlying soil is less steep than during the daytime. Therefore, the temperature acquired by the PMW sensor is closer to that acquired by the TIR sensor. The varying accuracies of the estimated

**Table 4**  
Root mean squared deviations (RMSDs) of the estimated LST based on AMSR-E data for different LC types. The numbers in brackets represent RMSDs for the methods proposed by Holmes et al. (2009).

| Land cover type             | Daytime    |            |             |             | Nighttime  |           |            |            |
|-----------------------------|------------|------------|-------------|-------------|------------|-----------|------------|------------|
|                             | Spring     | Summer     | Autumn      | Winter      | Spring     | Summer    | Autumn     | Winter     |
| Water and permanent wetland | 6.7        | 3.4        | 3.1         | 3.9         | 8.9        | 3.1       | 3.6        | 3.0        |
| Evergreen forest            | 2.1 (2.9)  | 2.7 (3.6)  | 1.9 (3.4)   | 2.0 (3.0)   | 1.4 (2.4)  | 4.4 (4.5) | 1.9 (3.5)  | 1.5 (2.5)  |
| Deciduous forest            | 3.2 (4.4)  | 2.2 (5.0)  | 2.3 (4.5)   | 2.9 (4.3)   | 3.4 (5.2)  | 2.1 (4.5) | 2.3 (5.0)  | 5.7 (5.1)  |
| Shrubland                   | 9.8 (13.2) | 8.2 (11.1) | 11.8 (12.2) | 12.8 (13.6) | 3.8 (5.1)  | 2.4 (4.4) | 4.8 (4.7)  | –          |
| Savanna and grassland       | 5.3 (8.0)  | 6.2 (6.6)  | 4.9 (7.5)   | 8.2 (10.0)  | 11.0 (7.6) | 2.5 (6.2) | 3.5 (6.0)  | 3.6 (4.2)  |
| Cropland                    | 5.2 (6.9)  | 2.5 (5.7)  | 2.2 (5.5)   | 2.6 (6.9)   | 2.3 (5.8)  | 3.1 (5.2) | 2.3 (5.9)  | 2.7 (9.1)  |
| Barren land                 | 6.6 (13.2) | 5.0 (10.4) | 5.6 (11.2)  | 8.6 (13.1)  | 4.6 (11.6) | 2.9 (9.7) | 3.6 (10.1) | 8.7 (13.0) |

LSTs of barren land are most likely caused by reasons similar to those affecting savanna and grassland.

The accuracies of the estimated surface temperatures of cropland are comparable to those of deciduous forest. The MAD value ranges from 1.7 K to 2.6 K and the RMSD value ranges from 2.2 K to 3.1 K under all conditions except the daytime cases in the spring. The mean values of daytime MAD and RMSD are 2.5 K and 3.2 K, respectively; the mean values of nighttime MAD and RMSD are 2.1 K and 2.6 K, respectively. The accuracies of the single band method proposed by Holmes et al. (2009) are lower than the TL-LUT method when estimating cropland LSTs.

#### Comparison with the in situ measured LSTs

The daily AMSR-E LSTs and in-situ measured LSTs at five sites (i.e., ANNI, D105, D110, Gaize, and BJ) in 2003 are derived. For comparison purpose, the MODIS LSTs from MYD11A1 products are also derived. It is in our expectation that AMSR-E has a better ability to overcome the weather influences than MODIS in generating daily LSTs. For these five sites, the numbers of daytime AMSR-E LSTs are 244, 244, 266, 268, and 265, respectively; the numbers of nighttime AMSR-E LSTs are 260, 244, 244, 245, and 244, respectively. The corresponding numbers for MODIS LSTs are 162, 144, 160, 221, and 157 in the daytime, and 210, 229, 230, 274, and 221 in the nighttime. Although the five sites in the Tibet Plateau are selected as a case study here, one can expect that AMSR-E can provide more frequent daily LSTs than MODIS in cloudy areas.

The daily LSTs from AMSR-E, in-situ measurements, and MODIS at these five sites in 2003 are shown in Fig. 7. Because the broadband emissivities in Eq. (1) are calculated based on the MYD11A1 products, the AMSR-E LSTs and ground LSTs with no matching MODIS emissivities are not shown. The sample sizes of AMSR-E and ground LSTs are listed in Table 5. Fig. 7 demonstrates that the AMSR-E LST is close to the ground LST and they have very similar intra-annual variations. Therefore, it can be concluded that the TL-LUT method has a good ability to capture the temporal variations of surface temperature at these sites. A closer look in Fig. 7 shows that the daytime AMSR-E LSTs have larger deviations from the ground LSTs than the nighttime ones. In the daytime, the AMSR-E LSTs are generally lower than the ground LSTs at ANNI, D105, D110, and BJ sites, which can be explained by a slightly higher thermal sampling depth of the PMW radiation (Parinussa et al., 2008). An inverse phenomenon appears for Gaize site, at which the daytime ground LSTs are lower than the AMSR-E LSTs as well as the MODIS LSTs. The overestimation of AMSR-E LST may be induced by urban warming of Gaize city, which is about 300 m in the east from Gaize site.

The deviation of AMSR-E LSTs from the ground LSTs is contributed by several sources. One source is the scale difference between the AMSR-E pixel and the footprint of the longwave radiation measurement. It is impossible to quantify the heterogeneity of LSTs within the AMSR-E pixel in this study, because dense LST measurements are unavailable. Therefore, we validate the AMSR-E LSTs against the ground LSTs through  $R^2$  and SEE. Please see Tables 5 and 6 for daytime and nighttime cases, respectively. The calculated  $R^2$  and SEE for these five sites confirm that good similarities exist between the AMSR-E and ground LSTs. For the whole year, the daytime  $R^2$  and SEE are 0.381–0.812 and 5.1–6.6 K, respectively; their mean values are 0.594 and 5.7 K, respectively. Furthermore, the TL-LUT method has different ability to provide AMSR-E LSTs with different accuracies. For the sites without urban influences (ANNI, D105, D110, and BJ), the SEE in summer is lower than in other seasons, revealing that high vegetation abundance can decrease the difference between AMSR-E LSTs and LSTs derived from surface longwave measurements. The SEE is greatest in the spring and winter, suggesting that the thermal sampling depth should be accounted when estimating the surface temperatures from AMSR-E

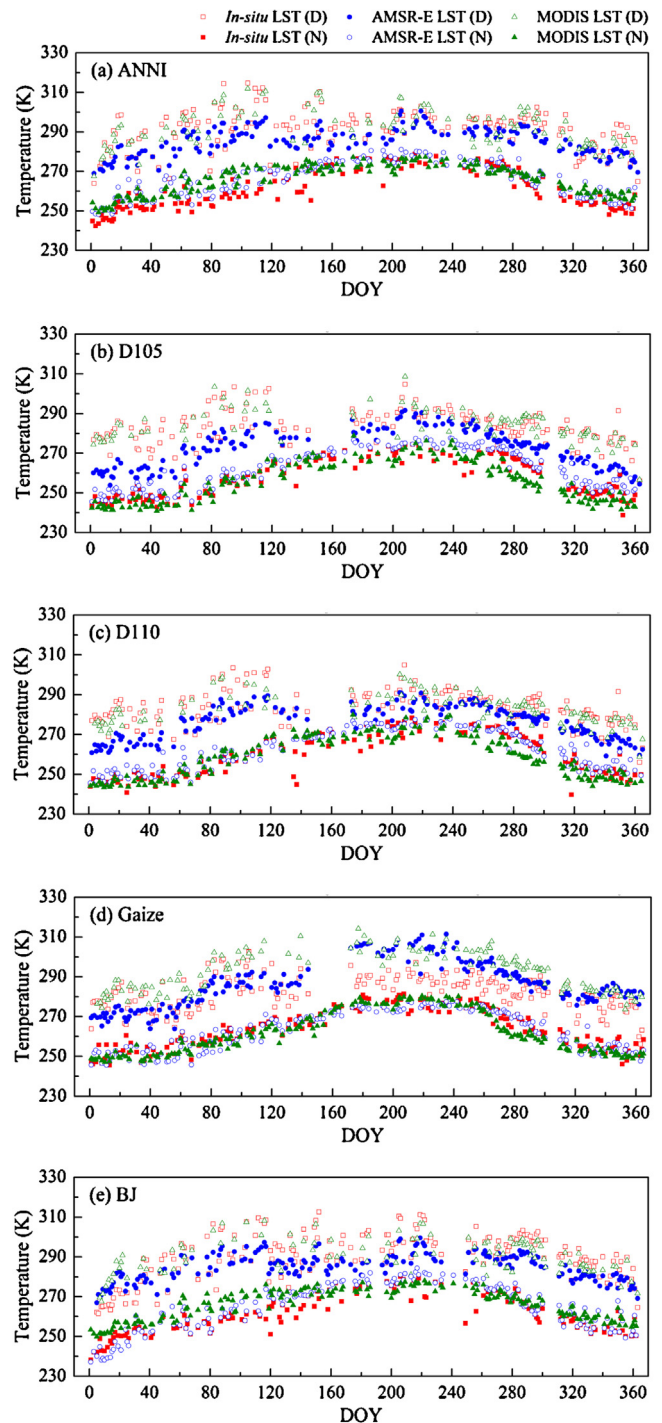


Fig. 7. The daily LSTs from AMSR-E, in-situ measurements, and MODIS at five sites (i.e., ANNI, D105, D110, Gaize, and BJ) in 2003. The symbols "D" and "N" mean daytime and nighttime, respectively.

data. The largest deviation appears at Gaize site, which is influenced by urban warming.

The nighttime AMSR-E LSTs exhibit better agreement with the ground LSTs than the daytime ones. For statistics on the whole year, all the nighttime  $R^2$  values are larger than 0.8 and the SEE values are lower than 4.5 K, suggesting a good consistency between AMSR-E and ground LSTs. The accuracy of the TL-LUT method also varies according to seasons. The lowest SEEs appear in summer, with SEEs of the five sites lower than 1.9 K.

**Table 5**  
 $R^2$  and SEE values of the regressions between the estimated LSTs and in-situ measured LSTs in daytime cases.

| Site  | Statistics  | Spring | Summer | Autumn | Winter | The whole year |
|-------|-------------|--------|--------|--------|--------|----------------|
| ANNI  | $R^2$       | 0.776  | 0.564  | 0.644  | 0.780  | 0.699          |
|       | SEE (K)     | 5.0    | 3.8    | 4.3    | 4.2    | 5.4            |
|       | Sample size | 47     | 35     | 46     | 45     | 173            |
| D105  | $R^2$       | 0.359  | 0.680  | 0.409  | 0.576  | 0.559          |
|       | SEE (K)     | 7.5    | 3.0    | 3.7    | 4.2    | 5.4            |
|       | Sample size | 35     | 28     | 52     | 43     | 158            |
| D110  | $R^2$       | 0.517  | 0.463  | 0.410  | 0.241  | 0.517          |
|       | SEE (K)     | 6.9    | 3.9    | 3.9    | 7.0    | 6.0            |
|       | Sample size | 37     | 34     | 57     | 47     | 175            |
| Gaize | $R^2$       | 0.190  | 0.031* | 0.418  | 0.001* | 0.381          |
|       | SEE (K)     | 8.1    | 4.1    | 4.0    | 6.5    | 6.6            |
|       | Sample size | 44     | 35     | 57     | 60     | 196            |
| BJ    | $R^2$       | 0.770  | 0.793  | 0.665  | 0.561  | 0.812          |
|       | SEE (K)     | 4.6    | 3.4    | 3.8    | 6.4    | 5.1            |
|       | Sample size | 51     | 37     | 53     | 49     | 190            |

\* All regressions are significant at 0.01 level except Gaize site in summer and autumn.

The calculated AMSR-E LSTs agree well with the MODIS LSTs to represent the daily variations of surface temperature, as shown in Fig. 7. The daytime MODIS LSTs are higher than the AMSR-E LSTs, due to higher thermal sampling depth of the PMW radiation. However, the AMSR-E and MODIS LSTs have good agreement in the nighttime, when the heterogeneity of LSTs within the AMSR-E footprints decreased. From examinations on the MODIS LSTs, we find that the MODIS observations over the Tibet Plateau are seriously contaminated by weather in summer. Therefore, it will be useful to estimate the LSTs with good accuracies from the AMSR-E data, as a substitute for MODIS LSTs in cloudy conditions.

#### Comparison with the meteorological observations

The daily maximum and minimum air temperatures ( $T_{a-max}$  and  $T_{a-min}$ , respectively) at 24 ground stations are used to evaluate the estimated AMSR-E LSTs. This evaluation is qualitative because the estimated LST has different physical meaning from the air temperature. However, the comparison is possible because the air temperature has close relationships with the LST, especially when the roughness length of the vegetation is high (Holmes et al., 2009). In addition, the overpass times of the AMSR-E sensor are approximately 13:30 and 01:30 at local solar time, which are near the times when  $T_{a-max}$  and  $T_{a-min}$  appear in a diurnal cycle.

The scatter plots between  $T_{a-max}$  and daytime AMSR-E LST and  $T_{a-min}$  and nighttime AMSR-E LST at the 24 meteorological stations of different land cover types are shown in Fig. 8. Close linear relationships apparently exist between  $T_{a-max}$  and daytime AMSR-E  $T_s$

LST and  $T_{a-min}$  and nighttime AMSR-E LST, demonstrating that the TL-LUT method has a good ability in capturing the daily variations of surface temperatures for different LC features.

For dense and high vegetation, e.g., forest, the PMW radiation observed by AMSR-E sensor is mainly from the canopy, the height of which is higher than the height for measuring the air temperatures. Therefore, the AMSR-E LST of forest (i.e., evergreen forest and deciduous forest) is slightly lower than  $T_{a-max}$  or  $T_{a-min}$ , shown by Fig. 8(a) and (b), especially in the daytime. For low vegetation, including savanna and grassland as well as cropland, most of the scatter points are near the 1:1 line, demonstrating the AMSR-E LST had closer relationships with the air temperature. For barren land, it is expected that the daytime AMSR-E LST is higher than  $T_{a-max}$ . The contrast between AMSR-E LST and  $T_{a-min}$  decreased during the nighttime except the barren land, which has much higher cool rate than the air in the night.

Due to different physical meanings of the air temperature and AMSR-E LST, regressions are conducted by selecting the  $T_{a-max}$  or  $T_{a-min}$  as the dependent variable and the AMSR-E LST as the independent variable. The daytime  $R^2$  ranges from 0.503 for the evergreen forest station to 0.923 for the deciduous forest stations; the nighttime  $R^2$  ranges from 0.533 for the evergreen forest station to 0.928 for the barren land stations. The statistics confirm the good relationships between  $T_{a-max}$  or  $T_{a-min}$  and AMSR-E LSTs. The lowest daytime and nighttime  $R^2$  of the evergreen forest station (Mengla, see Fig. 1), are resulted from large areas of open water after heavy precipitation.

**Table 6**  
 $R^2$  and SEE values of the regressions between the estimated LSTs and in-situ measured LSTs in nighttime cases.

| Site  | Statistics  | Spring | Summer | Autumn | Winter | The whole year |
|-------|-------------|--------|--------|--------|--------|----------------|
| ANNI  | $R^2$       | 0.271  | 0.433  | 0.879  | 0.627  | 0.805          |
|       | SEE (K)     | 4.5    | 1.9    | 2.4    | 3.2    | 3.8            |
|       | Sample size | 49     | 41     | 48     | 51     | 189            |
| D105  | $R^2$       | 0.874  | 0.814  | 0.898  | 0.581  | 0.898          |
|       | SEE (K)     | 2.2    | 1.1    | 2.4    | 2.3    | 3.1            |
|       | Sample size | 41     | 33     | 51     | 50     | 175            |
| D110  | $R^2$       | 0.851  | 0.750  | 0.902  | 0.563  | 0.886          |
|       | SEE (K)     | 2.4    | 1.2    | 2.3    | 2.4    | 3.3            |
|       | Sample size | 42     | 39     | 50     | 48     | 179            |
| Gaize | $R^2$       | 0.678  | 0.489  | 0.725  | 0.197  | 0.853          |
|       | SEE (K)     | 3.6    | 1.7    | 4.1    | 3.0    | 3.8            |
|       | Sample size | 51     | 42     | 49     | 55     | 197            |
| BJ    | $R^2$       | 0.485  | 0.761  | 0.921  | 0.851  | 0.851          |
|       | SEE (K)     | 4.6    | 1.4    | 2.2    | 3.1    | 4.5            |
|       | Sample size | 46     | 36     | 50     | 47     | 179            |

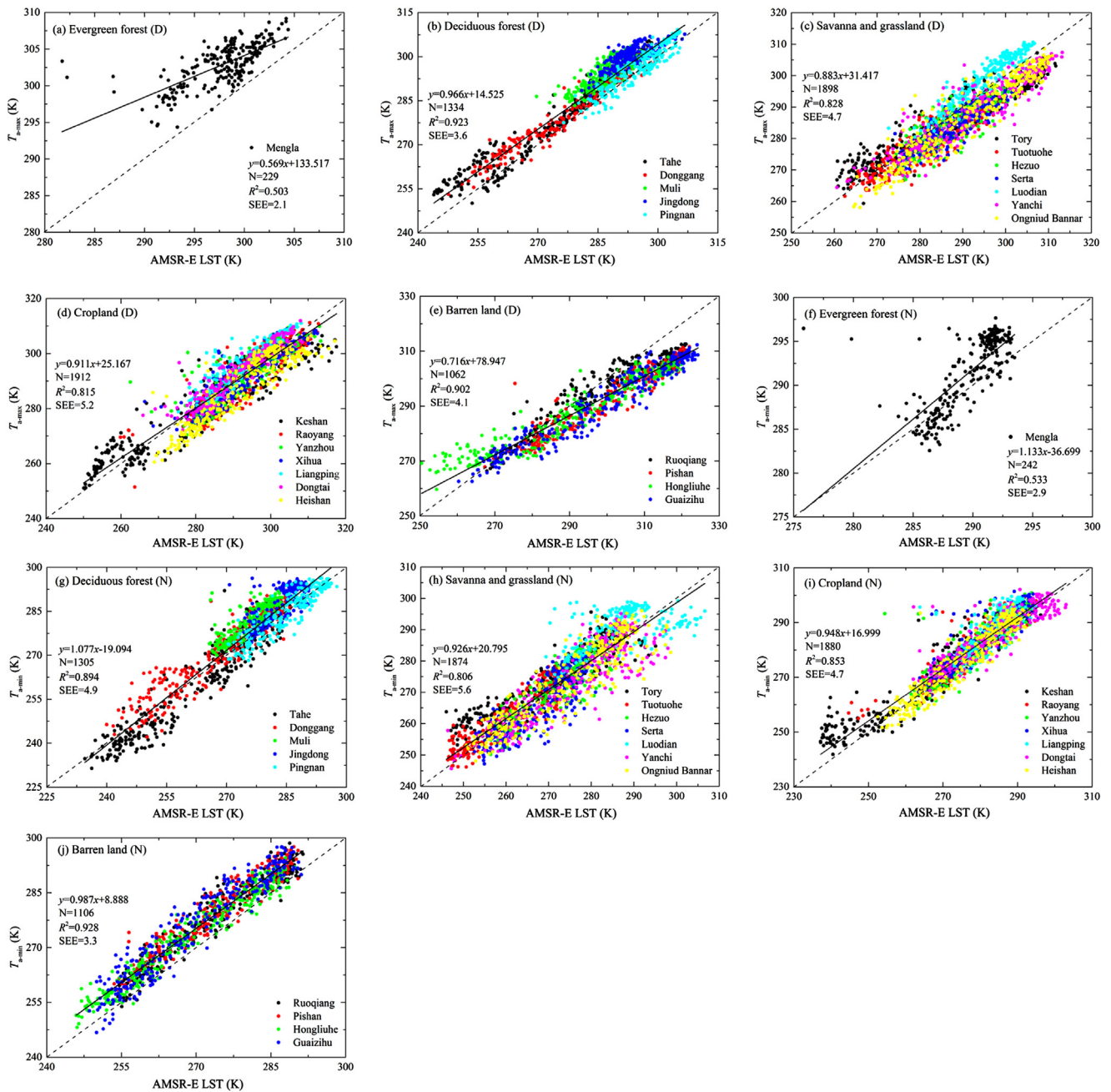


**Fig. 8.** Scatter plots between  $T_{a-max}$  and daytime AMSR-E LST and  $T_{a-min}$  and nighttime AMSR-E LST at ground stations of different land cover types. The symbols “D” and “N” mean daytime and nighttime, respectively. The dash line denotes the 1:1 line.

### Application of the TL-LUT method

The proposed TL-LUT method is applied to generate a LST time-series of the Chinese landmass. An example is given in Fig. 9, which shows the estimated daytime and nighttime LSTs on the 15th day of each month in 2003. The estimated LST is a good indicator of temperature patterns on the Chinese landmass. In the annual cycle, the land surface became increasingly warmer from January to June and then got increasingly colder from July onward. In general, the land surface was warmer in the daytime than in the nighttime. The spatial patterns of the LST and the diurnal temperature range were closely linked to land cover and elevation.

### Discussion

The aforementioned TL-LUT method is based on different apparent PMW signatures of different LC types. These signatures vary according to their physical variations during the daytime and nighttime in different seasons. The advantages of this method include the following. First, the LST provided by MODIS is selected as the dependent variable; therefore, the nominal physical meaning of the estimated temperature from the AMSR-E data is surface temperature, which refers to the area-weighted average of the temperatures of the various land covers within a specific scene (Holmes et al., 2009). In this way, the estimated AMSR-E LST would be a

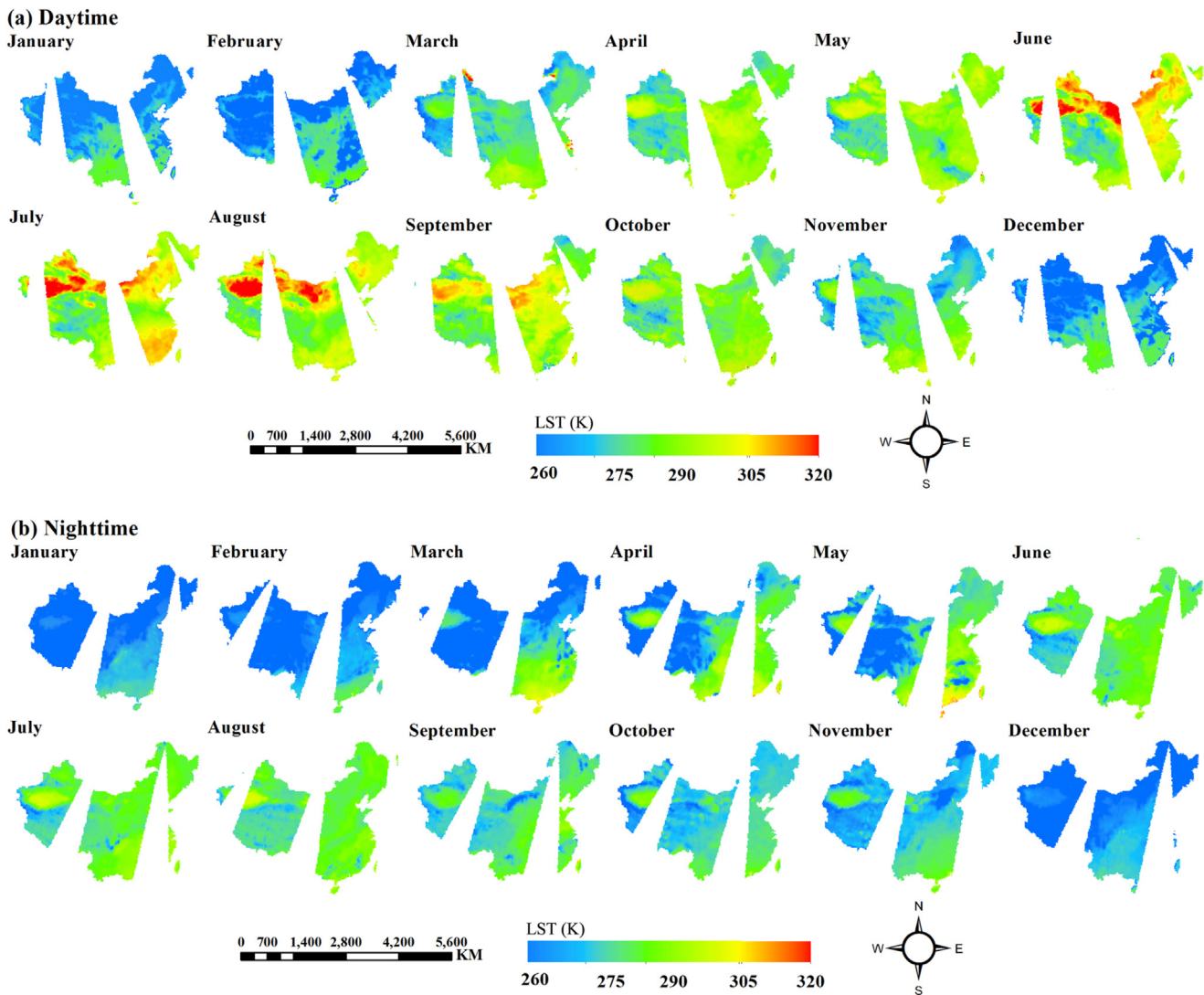


Fig. 9. Estimated daytime and nighttime AMSR-E LSTs of the Chinese landmass on the 15th day of each month in 2003.

convenient input parameter for current land process models as the TIR LST. Second, all the brightness temperatures, along with certain band combinations, are used as potential predictors in the TL-LUT method, and their inclusion in the eventual retrieval equation depend on their ability to describe the variations of the LST or to overcome atmospheric and emissivity effects. Assessments of the method demonstrate that more predictors yield better estimation accuracy compared to the single channel method, in which the 36.5 GHz vertical polarized channel is commonly used. Third, this method takes full advantage of the fact that both the AMSR-E and MODIS sensors are onboard the Aqua satellite and that different surface information sources, including the PMW, TIR, and VNIR (visible and near infrared) signatures, are utilized to better understand the PMW features of different surfaces. Although the AMSR-E sensor has not produced any data since October 2011, the A-Train or the Afternoon Constellation organized by NASA and its international partners provide the possibility for integrating Earth observations in VNIR, TIR and PMW spectral regions. In addition, the integration of PMW data and land cover data provide a better opportunity to examine the PMW signatures of different LC types in different meteorological conditions. Although the yearly MODIS LC products are used in the TL-LUT method, its influence induced by low temporal resolution is mitigated by treating the AMSR-E images in different seasons separately.

The thermal sampling depth is an important factor influencing the source that contributes to the detected PMW radiation at ground level. For the TIR band, the thermal sampling depth ranges from several micrometers to tens of micrometers, but for the PMW band, this depth varies according to surface moisture, frequency, and other factors. The difference between TIR and PMW thermal sampling depths is one of the most important difficulties in integrating the TIR and PMW remote sensing data. For dense vegetation in a homogenous footprint, the PMW surface temperature is close to that of TIR. However, this problem becomes more complicated for barren land and surfaces with sparse vegetation. In such cases, the variation in surface temperatures cannot be sufficiently explained and modeled by the brightness temperatures at different frequencies. Our preliminary research on the practical model for converting the AMSR-E LST and MODIS LST to each other in the Tibet Plateau demonstrates that heat conduction models are beneficial in solving this difficulty (Zhan et al., 2014; Zhang, 2014).

Assessment of the AMSR-E LSTs faces much more difficulties than that of the TIR LSTs due to the coarse spatial resolution. The errors of the validating LSTs result many sources, e.g., uncertainties of the reference LSTs, scale miss-matches, errors with the retrieval method, and the precision of the PMW sensor. Validation with the synchronous MODIS LST products in 2011 is beneficial in minimizing the scale miss-matches and testing whether the

TL-LUT method can generate AMSR-E LSTs with comparable accuracies as the MODIS LSTs. Uncertainties remain in the comparison between the in-situ measured LSTs and AMSR-E LSTs at five sites in the Tibet Plateau. However, the comparison still exhibits the ability of the TL-LUT method in capturing the intra-annual variations of temperature in surfaces with extremely low vegetation, especially in nighttime conditions. The accuracies at these sites are encouraging. Therefore, AMSR-E LSTs generated from the TL-LUT method are expected to play important role in analyzing the climate changes in the Tibet Plateau, which is the current focus of global climate change. Additional comparison with the in-situ measured air temperatures is influenced by its low temporal resolution and different physical meaning from the AMSR-E LST. However, good agreements between the AMSR-E LSTs and the air temperatures exhibit the ability of the generated AMSR-E LSTs in representing the spatial patterns of the LSTs in the entire Chinese landmass.

## Conclusions

PMW remote sensing provides a good data source for estimating the LSTs in cloudy regions by overcoming the disturbances from cloud cover, aerosol, and rain. Significant linear or approximately linear relationships exist between the surface temperatures and PMW brightness temperatures at different frequencies. A temporally land cover based look-up table (TL-LUT) method is proposed in this research to estimate LSTs from the AMSR-E data over the Chinese landmass. One major advantage of this method is that the utilized retrieval equation depends on the temporal condition and LC type, to account the variations of the physical characteristics of land surface and their dynamic influences on the above-mentioned relationships. All the daily AMSR-E images and daily MYD11A1 LST products covering the entire Chinese landmass in 2010 are used to train this method. Therefore, this method has another advantage in its good spatial representativeness and stable performance.

Comprehensive assessments of the proposed method are conducted based on the synchronous MODIS LST products covering the country in 2011, the in-situ measured LSTs at five sites in the Tibet-Plateau in 2003, and the air temperatures from 24 stations distributed in China in 2003. Results demonstrate that the TL-LUT method has a good ability in estimating surface temperatures of water and permanent wetland, evergreen forest, deciduous forest, and cropland. When compared with the MODIS LSTs, the MADs and RMSDs of water and permanent wetland are better than 2.7 K and 3.9 K in summer, autumn, and winter. For the evergreen forest, the daytime and nighttime accuracies in the whole year are better than 2.2 K and 2.3 K, respectively. For the deciduous forest, the daytime and nighttime accuracies in the whole year are better than 2.7 K and 2.4 K, respectively. The corresponding accuracies for the cropland are better than 3.2 K and 2.6 K, respectively. Although the estimated AMSR-E LSTs of the other types have lower accuracies, the estimated surface temperatures show strong correlations with the MODIS LSTs. From the comparison, we find that the proposed TL-LUT method performs better in retrieving LSTs with AMSR-E data than the method that uses a single brightness temperature in 36.5 GHz vertical polarization channel.

When compared with the in-situ measured LSTs at four sites without urban warming in the Tibet Plateau, the SEEs between the estimated AMSR-E LST and in-situ measured LST are from 5.1 K to 6.0 K in the daytime and 3.1 K to 4.5 K in the nighttime. Further comparison with the in-situ measured air temperatures at 24 Chinese meteorological stations confirms the good performance of the TL-LUT method. The feasibility of PMW remote sensing in estimating the LST for China can complement the TIR data and can, therefore, aid in the generation of daily LST maps for the entire country.

## Acknowledgments

This work was supported in part by the Chinese State Key Basic Research Project (Grant number: 2013CB733406), by the National Natural Science Foundation of China (Grant numbers: 41371341, 41101380, and 41371399), by the Opening Funding of State Key Laboratory for Remote Sensing Science (Grant number: OFSLRSS201313), and by the 2012 Undergraduate Innovative Training Program of University of Electronic Science and Technology of China. We also want to thank the anonymous referees for their constructive criticism and comments.

## References

- Basist, A., Grody, N.C., Peterson, T.C., 1998. Using the Special Sensor Microwave/Imager to monitor land surface temperatures, wetness, and snow cover. *J. Appl. Meteorol.* 37, 888–911.
- Becker, F., Li, Z.L., 1990. Towards a local split window method over land surfaces. *Int. J. Remote Sens.* 11 (3), 369–393.
- Chen, S.S., Chen, X.Z., Chen, W.Q., 2011. A simple retrieval method of land surface temperature from AMSR-E passive microwave data – a case study over Southern China during the strong snow disaster of 2008. *Int. J. Appl. Earth Observ. Geoinf.* 13 (1), 140–151.
- Dash, P., Göttsche, F.M., Olesen, F.S., Fischer, H., 2002. Land surface temperature and emissivity estimation from passive sensor data: theory and practice – current trends. *Int. J. Remote Sens.* 23 (13), 2563–2594.
- Fily, M., Royer, A., Goita, K., 2003. A simple retrieval method for land surface temperature and fraction of water surface determination from satellite microwave brightness temperatures in sub-arctic areas. *Remote Sens. Environ.* 85 (3), 328–338.
- Frey, C.M., Kuenzer, C., Dech, S., 2012. Quantitative comparison of the operational NOAA-AVHRR LST product of DLR and the MODIS LST product V005. *Int. J. Remote Sens.* 33 (22), 7165–7183.
- Gao, H.L., Fu, R., Dickinson, R.E., 2008. A practical method for retrieving land surface temperature from AMSR-E over the Amazon forest. *IEEE Trans. Geosci. Remote Sens.* 46 (1), 193–199.
- Gillespie, A.T., Rokugawa, S., Hook, S., 1998. Temperature emissivity separation from Advanced Spaceborne Thermal Emission and Reflection Radiometer (ASTER) images. *IEEE Trans. Geosci. Remote Sens.* 36 (4), 1113–1126.
- Holmes, T.R.H., De Jeu, R.A.M., Owe, M., Dolman, A.J., 2009. Land surface temperature from Ka band (37 GHz) passive microwave observations. *J. Geophys. Res.* 114 (D04113), <http://dx.doi.org/10.1029/2008JD010257>.
- Jia, Y.Y., Li, Z.L., 2006. Progress in land surface temperature retrieval from passive microwave remotely sensed data. *Prog. Geogr.* 25 (3), 96–105.
- Jiménez-Muñoz, J.C., Sobrino, J.A., 2003. A generalized single-channel method for retrieving land surface temperature from remote sensing data. *J. Geophys. Res.* 108, <http://dx.doi.org/10.1029/2003JD003480>.
- Li, W.B., Zhu, Y.J., Hong, G., 1998. Remote sensing of surface temperature from SSM/I in eastern China. *Prog. Nat. Sci.* 8 (3), 305–313.
- Li, Z.L., Tang, B.H., Wu, H., Ren, H.Z., Yan, G.J., Wan, Z.M., Trigo, I.F., Sobrino, J.A., 2013. Satellite-derived land surface temperature: current status and perspectives. *Remote Sens. Environ.* 131, 14–37.
- Liang, S.L., 2004. *Quantitative Remote Sensing of Land Surfaces*. John Wiley & Sons, New Jersey, pp. 388.
- Mcfarland, M.J., Miller, R.L., Neale, C.M.U., 1990. Land surface temperature derived from the SSM/I passive microwave brightness temperatures. *IEEE Trans. Geosci. Remote Sens.* 28 (5), 839–845.
- Owe, M., Van De Griend, A.A., 2001. On the relationship between thermodynamic surface temperature and high-frequency (37 GHz) vertically polarized brightness temperature under semi-arid conditions. *Int. J. Remote Sens.* 22 (17), 3521–3532.
- Prigent, C., Rossow, W.B., Matthews, E., Marticorena, B., 1999. Microwave radiometric signatures of different surface types in deserts. *J. Geophys. Res.* 104 (D10), 12147–12158.
- Parinussa, R.M., De Jeu, R.A.M., Holmes, T.R.H., Walker, J.P., 2008. Comparison of microwave and infrared land surface temperature products over the NAFE'06 research sites. *IEEE Geosci. Remote Sens. Lett.* 5 (4), 783–787.
- Qin, Z., Karnieli, A., Berliner, P., 2001. A mono-window algorithm for retrieving land surface temperature from Landsat TM data and its application to the Israel–Egypt border region. *Int. J. Remote Sens.* 22 (18), 3719–3746.
- Royer, A., Poirier, S., 2010. Surface temperature spatial and temporal variations in North America from homogenized satellite SMMR-SSM/I microwave measurements and reanalysis for 1979–2008. *J. Geophys. Res.* 115 (D8), <http://dx.doi.org/10.1029/2009JD012760>.
- Snyder, W.C., Wan, Z., Zhang, Y., Feng, Y.Z., 1998. Classification-based emissivity for land surface temperature measurement from space. *Int. J. Remote Sens.* 19 (14), 2753–2774.
- Salama, M.S., Van der Velde, R., Zhong, L., 2012. Decadal variations of land surface temperature anomalies observed over the Tibetan Plateau by the Special Sensor Microwave Imager (SSM/I) from 1987 to 2008. *Clim. Change* 114 (3–4), 769–781.

- Wan, Z.M., Dozier, J., 1996. A generalized split-window algorithm for retrieving land-surface temperature from space. *IEEE Trans. Geosci. Remote Sens.* 34 (4), 892–905.
- Wan, Z.M., 2008. New refinements and validation of the MODIS land-surface temperature/emissivity products. *Remote Sens. Environ.* 112, 59–74.
- Wan, Z.M., 2014. New refinements and validation of the collection-6 MODIS land-surface temperature/emissivity product. *Remote Sens. Environ.* 140, 36–45.
- Xu, J., Haginoya, S., 2001. An estimation of heat and water balances in the Tibetan Plateau. *J. Meteorol. Soc. Japan.* 79, 485–504.
- Zhan, W.F., Zhou, J., Ju, W.M., Li, M.C., Sandholt, I., Voogt, J., Yu, C., 2014. Remotely sensed soil temperatures beneath snow-free skin-surface using thermal observations from tandem polar-orbiting satellites: an analytical three-time-scale model. *Remote Sens. Environ.* 143, 1–14.
- Zhou, J., Chen, Y.H., Wang, J.F., Zhan, W.F., 2011a. Maximum nighttime urban heat island (UHI) intensity simulation by integrating remotely sensed data and meteorological observations. *IEEE J. Sel. Top. Appl. Earth Observ.* 4 (1), 138–146.
- Zhou, J., Li, J., Zhao, X., Zhan, W.F., Guo, J.X., 2011b. A modified single-channel algorithm for land surface temperature retrieval from HJ-1B satellite data. *J. Infrared Millim. Waves* 30 (1), 61–67.
- Zhou, J., Li, J., Zhang, L.X., 2012. Intercomparison of methods for estimating land surface temperature from a Landsat-5 TM image in an arid region with low water vapour in the atmosphere. *Int. J. Remote Sens.* 33 (8), 2582–2602.
- Zhou, J., Chen, Y.H., Zhang, X., Zhan, W.F., 2013. Modelling the diurnal variations of urban heat islands with multi-source satellite data. *Int. J. Remote Sens.* 34 (21), 7568–7588.
- Zhou, J., Zhang, X., Zhan, W.F., Zhang, H.L., 2014. Land surface temperature retrieval from MODIS data by integrating regression models and the genetic algorithm in an arid region. *Remote Sens.* 6, 5344–5367.
- Zhang, X.D., (Bachelor Dissertation) 2014. Simulation and Analysis on the MODIS Skin Temperature and AMSR-E Effective Surface Temperature. University of Electronic Science and Technology of China.